Hearing Research 390 (2020) 107933

Contents lists available at ScienceDirect

Hearing Research

journal homepage: www.elsevier.com/locate/heares

Research Paper

Volume gradients in inner hair cell-auditory nerve fiber pre- and postsynaptic proteins differ across mouse strains

Daniël O.J. Reijntjes [a, *], Christine Köppl [b], Sonja J. Pyott [a]

[a] University of Groningen, University Medical Center Groningen, Groningen, Department of Otorhinolaryngology and Head/Neck Surgery, 9713 GZ, Groningen, the Netherlands

[b] Cluster of Excellence "Hearing4all" and Research Centre Neurosensory Science, Department of Neuroscience, School of Medicine and Health Science, Carl von Ossietzky University Oldenburg, Germany

ARTICLE INFO

Article history:
Received 6 August 2019
Received in revised form
12 February 2020
Accepted 26 February 2020
Available online 6 March 2020

ABSTRACT

In different animal models, auditory nerve fibers display variation in spontaneous activity and response threshold. Functional and structural differences among inner hair cell ribbon synapses are believed to contribute to this variation. The relative volumes of synaptic proteins at individual synapses might be one such difference. This idea is based on the observation of opposing volume gradients of the presynaptic ribbons and associated postsynaptic glutamate receptor patches in mice along the pillar modiolar axis of the inner hair cell, the same axis along which fibers were shown to vary in their physiological properties. However, it is unclear whether these opposing gradients are expressed consistently across animal models. In addition, such volume gradients observed for separate populations of presynaptic ribbons and postsynaptic glutamate receptor patches suggest different relative volumes of these synaptic structures at individual synapses; however, these differences have not been examined in mice. Furthermore, it is unclear whether such gradients are limited to these synaptic proteins. Therefore, we analyzed organs of Corti isolated from CBA/CaJ, C57BL/6, and FVB/NJ mice using immunofluorescence, confocal microscopy, and quantitative image analysis. We find consistent expression of presynaptic volume gradients across strains of mice and inconsistent expression of postsynaptic volume gradients. We find differences in the relative volume of synaptic proteins, but these are different between CBA/CaJ mice, and C57BL/6 and FVB/NJ mice. We find similar results in C57BL/6 and FVB/NJ mice when using other postsynaptic density proteins (Shank1, Homer, and PSD95). These results have implications for the mechanisms by which volumes of synaptic proteins contribute to variations in the physiology of individual auditory nerve fibers and their vulnerability to excitotoxicity.

© 2020 The Authors. Published by Elsevier B.V. This is an open access article under the CC BY-NC-ND license (http://creativecommons.org/licenses/by-nc-nd/4.0/).

1. Introduction

Auditory nerve fibers carry all acoustic information from the sensory hair cells in the cochlea to the brain. Each type I auditory nerve fiber makes one synaptic connection to an inner hair cell, and each inner hair cell is innervated by between ten and twenty type I auditory nerve fibers (for review, see, e.g., Meyer and Moser, 2010). The type I auditory nerve fibers are stimulated when glutamate, released from the presynaptic ribbons in the inner hair cells, activates glutamate receptors on the postsynaptic auditory nerve fiber terminal (Glowatzki and Fuchs, 2002).

Experimental findings from various mammalian species indicate that subgroups of type I auditory nerve fibers can be distinguished by differences in their physiology, anatomy, and vulnerability to damage (for review, see, e.g., Heil and Peterson, 2015). In particular, differences in spontaneous firing rates define at least two subgroups with low or high spontaneous firing rates in a variety of mammals (rat: Barbary, 1991; rabbit: Borg et al., 1988; cat: Liberman, 1978; Merchan-Perez and Liberman, 1996; gerbil: Ohlemiller et al., 2005; Schmiedt, 1989; CBA/CaJ and C57BL/6 mice: Taberner and Liberman, 2005; guinea pig: Winter et al., 1990). In cat, spontaneous firing rate correlates with the side of innervation on the inner hair cells. Specifically, when dividing the inner hair cells by a central axis into a pillar and a modiolar side, high spontaneous rate fibers contact the pillar side and low spontaneous rate fibers contact the modiolar side (Fig. 1; Liberman, 1982; Liberman

* Corresponding author.
E-mail address: dreijnt1@jhmi.edu (D.O.J. Reijntjes).

https://doi.org/10.1016/j.heares.2020.107933
0378-5955/© 2020 The Authors. Published by Elsevier B.V. This is an open access article under the CC BY-NC-ND license (http://creativecommons.org/licenses/by-nc-nd/4.0/).

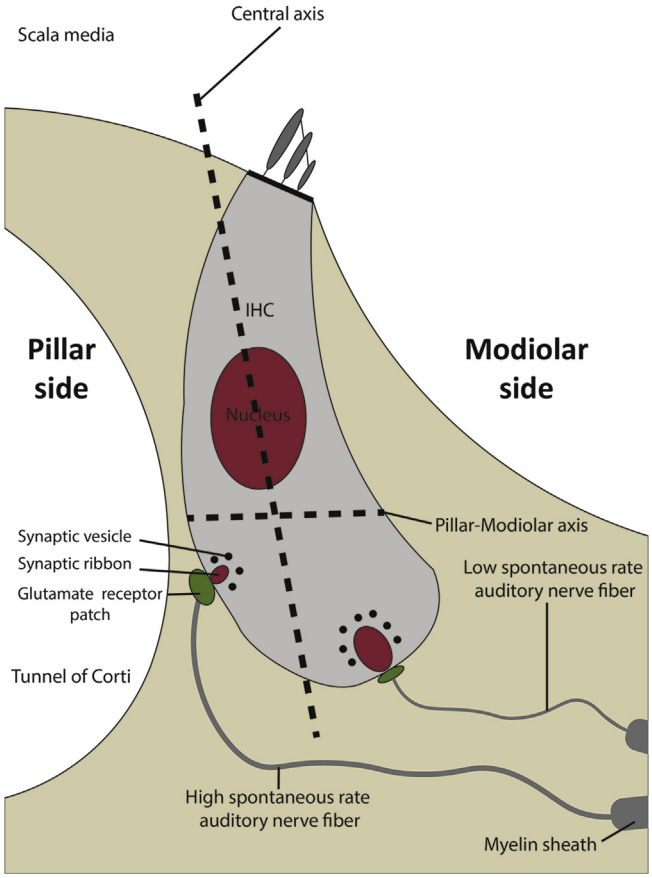

Fig. 1. Schematic of the inner hair cell-auditory nerve fiber synapses. Each inner hair cell (IHC) forms synapses with ten to twenty auditory nerve fibers of which two are depicted. Functional differences between auditory nerve fibers have been correlated to the spatial location of their sites of contact with the IHCs (pillar or modiolar facing, Liberman, 1982). Based on work in CBA/CaJ mice (Liberman et al., 2011), opposing volume gradients in pre- and postsynaptic proteins are hypothesized to underlie these functional differences. Specifically, synapses on the modiolar side of the IHC have relatively larger presynaptic CTBP2-containing ribbons (which serve to tether synaptic vesicles and are shown in red) and smaller postsynaptic GluA2-containing glutamate receptor patches (shown in green) and the reverse trend is seen in synapses on the pillar side of the IHC. These spatial differences can be examined by separating the visualized synapses by defining a central axis for which we used the IHC nucleus. (The nucleus is co-labelled by the antibody for CTBP2, as can be seen in subsequent micrographs, and is therefore similarly depicted in red, see methods). This work examined whether these gradients in presynaptic ribbon and postsynaptic protein volumes could be observed in two other commonly used strains of mice, FVB/NJ and C57BL/6. (For interpretation of the references to colour in this figure legend, the reader is referred to the Web version of this article.)

and Oliver, 1984; Merchan-Perez and Liberman, 1996).

The volume of glutamate-releasing presynaptic ribbons and postsynaptic glutamate receptor patches is thought to contribute to shaping these subgroups (Liberman et al., 2011). In several mammals, the ribbon volume is larger in auditory nerve fiber synapses on the modiolar side than in auditory nerve fiber synapses on the pillar side (mice: Gilels et al., 2013; Liberman et al., 2011; Liberman and Liberman, 2016; Paquette et al., 2016; Yin et al., 2014; guinea pig: Furman et al., 2013; rat: Kalluri and Monges-Hernandez, 2017; cat: Merchan-Perez and Liberman, 1996; gerbil: Zhang et al., 2018; and mole rat: Barone et al., 2019). In addition, in CBA/CaJ mice, the postsynaptic glutamate receptor volume is smaller in auditory nerve fibers contacting the modiolar side than in auditory nerve fibers contacting the pillar side (Liberman et al., 2011). These opposing differences in volume of the ribbons and glutamate receptor patches along the pillar-modiolar axis of the inner hair cell are dubbed opposing volume gradients. These volume gradients are suggested to represent structural differences in presynaptic and postsynaptic morphology between pillar and modiolar synapses contacting the inner hair cells that could contribute to shaping afferent fiber activity (Liberman et al., 2011).

It remains unclear to what extent these volume gradients are consistently expressed across animal models and, therefore, whether such volume gradients could indeed contribute to shaping afferent fiber activity. In guinea pig, no glutamate receptor volume gradient was observed (Furman et al., 2013), and, in gerbil, an observed glutamate receptor volume gradient was concurrent to the ribbon volume gradient instead of opposing (Zhang et al., 2018).

Moreover, in mice, volume gradients were originally identified by comparing the mean volume of ribbons and glutamate receptor patches on either side of the inner hair cell central axis (Liberman et al., 2011) and later confirmed to be gradual changes in the two populations of pre- and postsynaptic proteins from larger samples of inner hair cells (e.g., Yin et al., 2014). However, population gradients in the volumes of the presynaptic ribbons and postsynaptic glutamate receptor patches across the central axis of a group of inner hair cells do not *per se* indicate that there are structural differences in the pre- and postsynaptic morphology between individual pillar and modiolar synapses. Such structural differences would be revealed by examining correlations between the paired presynaptic ribbon and postsynaptic glutamate receptor patch volume of individual synapses. Inverse correlations would match structural differences implied by the opposing gradient whereas positive correlations would match structural differences implied by concurrent volume gradients. In gerbil, where the volume gradients are concurrent, ribbon volume indeed correlates positively to the volume of the glutamate receptor patch for individual synapses (Zhang et al., 2018). In mice, such correlations have not been studied.

Finally, structural differences in pre- and postsynaptic morphology might be expected to extend to other synaptic proteins, especially proteins that regulate expression of the postsynaptic glutamate receptors. Gradients in the volume of other synaptic proteins besides CTBP2, a component of the presynaptic ribbon, and GluR2, a component of the glutamate receptor patches, have not been investigated. Therefore, the aim of this study was threefold: 1) to determine whether opposing volume gradients are detectable in other strains of mice, specifically C57BL/6 and FVB/NJ; 2) to correlate presynaptic ribbon with postsynaptic glutamate receptor patch volumes for individual pillar and modiolar synapses in these two mouse strains; and 3) to examine whether other postsynaptic density proteins, including Shank1, Homer, and PSD95, showed volume gradients similar to the volume gradients observed for glutamate receptor patches in these two strains.

Using immunostaining, confocal microscopy, and quantitative image analysis, we find that in these strains of mice the direction of the gradients varies and is established by a subset of synapses. These findings need to be considered when evaluating the contributions of these gradients to variations in spontaneous activity and susceptibility to excitotoxicity among subgroups of auditory synapses.

2. Materials and methods

2.1. Animals

Mice from three different strains were used. In total, 16 C57BL/6 and 22 FVB/NJ mice were obtained from the breeding facilities at the University Medical Centre Groningen, the Netherlands, and 5 CBA/CaJ mice were obtained from the breeding facilities at the Carl von Ossietzky University Oldenburg, Germany. These three strains

were chosen because the FVB/NJ is another commonly used good hearing strain (Kommareddi et al., 2015), because the C57BL/6 is a commonly used strain for genetic manipulations but has a genetic defect that causes early onset hearing loss (Kane et al., 2012), and because volume gradients were originally observed in the good hearing CBA/CaJ mouse strain (Liberman et al., 2011), which were therefore used as controls. Mice were of either sex and between six and eight weeks of age. C57BL/6 and FVB/NJ mice were anesthetized by exposure to 4% isofluorane gas and decapitated. CBA/CaJ mice were euthanized by intraperitoneal injection with an overdose of sodium pentobarbital ("Narcoren", Merial GmbH, Hallbergmoos, Germany) and decapitated. Cochleae were dissected from the skull in ice cold PBS immediately after decapitation. A small hole was made in the cochlea over the apical turn, and the cochleae placed in ice cold 4% paraformaldehyde (Thermo-Fisher scientific) for 1 h (2 h for Shank1 immunolabeling). Organs of Corti were subsequently dissected from the cochleae in ice cold PBS and placed in goat blocking buffer (PBS with 5% normal goat serum and 4% Triton X-100) for at least 1 h at room temperature. All animal experiments were approved and conducted either in accordance with Dutch or German animal welfare laws.

2.2. Immunohistochemistry

To visualize the pre- and postsynaptic structures of the inner hair cell-auditory nerve fiber synapses, organs of Corti were double immunolabeled for a presynaptic protein and one of four postsynaptic proteins (Table 1). In some samples, a hair cell marker was added as a third immunolabel to visually assess whether the central axis was correctly positioned by the software to match the illustration in Fig. 1 (see section 2.5). Organs of Corti were incubated overnight (12–24 h) at room temperature in primary antibody diluted in goat blocking buffer. Subsequently, samples were incubated in secondary antibody diluted in goat blocking buffer (Table 1). After each incubation step, samples were rinsed three times in PBS with 0.2% Triton X-100 for 10 min each. Following the final rinse, organs of Corti were microdissected into two pieces to avoid overlap of the apical and the more basal turns and mounted in Vectashield mounting medium (Vector laboratories).

2.3. Image acquisition and processing

In order to localize specific cochlear frequency regions, cochlear frequency maps were generated for each organ of Corti using a freely available ImageJ plug-in from the Eaton-Peabody laboratories and the previously published place-frequency map (Müller et al., 2005). Low magnification images of all sections of the organ of Corti were captured using an epifluorescent microscope (Leica DM4000b) with a 5x dry NA 0.15 objective and Leica Application Suite (LAS) 4.3 software. When necessary, these images were stitched together in "FIJI" (Schindelin et al., 2012, https://imagej.net/Fiji) using the MosaicJ plug-in (Thévenaz and Unser, 2007).

In order to capture high resolution images of the inner hair cells and their synapses, specific frequency regions of the organ of Corti were scanned with a confocal microscope (Leica Microsystems CMS GmbH, Leica TCS SP8 system with a 63x oil, NA 1.4, objective, using LAS X software). High resolution micrographs were obtained for the 8, 16, and 32 kHz regions of one organ of Corti per mouse. These three frequencies were chosen to correspond to low, middle, and high cochlear frequencies in mouse. Each image contained about ten inner hair cells along with their synaptic proteins. Micrographs were scanned with a resolution of 0.09 μm per pixel at z-steps of 0.3 μm and a laser speed of 100 Hz. Fluorophores were excited by either a 488 OPSL, 552 OPSL, or 638 diode laser. Detection bandwidths were set at 20 nm for all three fluorophores (510–530 nm, 590–610 nm, 660–680 nm). Scans were performed sequentially with the 488 OPSL and the 638 diode laser on channel 1 and the 552 OPSL laser on channel 2. Confocal z-stacks were deconvolved with Huygens Professional software version 17.04 (Scientific Volume Imaging, The Netherlands, http://svi.nl) using the classic maximum likelihood algorithm with the signal to noise ratio = 20, maximum iterations = 40, quality threshold = 0.1, background per channel = 1, search for background = near/in object, and with a theoretical point spread function based on known microscope parameters for the Leica SP8 system.

2.4. Volume quantification of pre- and postsynaptic proteins

To quantify the volume of pre-and postsynaptic proteins, 3D reconstructions of the z-stacks were created in Imaris (version 7.6.4; Bitplane AG, Zurich, Switzerland). Volumes were obtained using the "surface" function in Imaris for the fluorescent signal of the nuclei and the pre- and postsynaptic proteins that were visualized as specific puncta. The surface function uses a two-step background subtraction/threshold selection procedure to detect surfaces. The obtained volume correlates with the summed

Table 1
Primary and secondary antibodies applied for fluorescent labelling of synaptic markers in the organ of Corti.

	Structure	Protein	Antibody type	Isotype	Origin	Concentration
Primary antibodies	Presynaptic ribbon protein (also labels the inner hair cell nucleus)	CTBP2	mouse monoclonal	IgG_1	BD Biosciences cat. no. 612044	0.83 μg/ml (1:300)
	Postsynaptic Glutamate receptor	GluA2	mouse monoclonal	IgG_{2a}	Millipore cat. no. MAB 397	7.1 μg/ml (1:300)
	Postsynaptic density scaffold protein	Shank1a C-terminus	rabbit polyclonal		Neuromics cat. no. RA19016	3.4 μg/ml (1:300)
	Postsynaptic density scaffold protein	Homer1/2/3	rabbit polyclonal		Synaptic Systems cat. no. 160 103	3.33 μg/ml (1:300)
	Postsynaptic density scaffold protein	PSD95	mouse monoclonal	IgG_{2a}	Neuromab cat. no. 75-028	3.43 μg/ml (1:300)
	Inner hair cell protein	Myosin 7A	rabbit polyclonal,		Proteus Biosciences cat. no. 25-6790	1 μg/ml (1:1000)[P]
	Inner hair cell protein	Myosin 7A	mouse monoclonal	IgG_{2a}	Santa Cruz biotech. cat. no. sc-74516	0.4 μg/ml (1:500)[P]
	Host species	**Target species**	**Conjugate**	**Isotype**	**Origin**	**Concentration**
Secondary antibodies	Goat	Anti mouse	alexa fluor 488	IgG1	Invitrogen cat. no. A-21121	4 μg/ml (1:500)
	Goat	Anti rabbit	alexa fluor 568		Invitrogen cat. no. A-11011	4 μg/ml (1:500)
	Goat	Anti mouse	alexa fluor 647	IgG2a	Invitrogen cat. no. A-21241	4 μg/ml (1:500)

[P] = Inner hair cell labeling was only used to ascertain that the plotted plane more or less bisected the row of inner hair cells.

fluorescent intensity within the volumes demarcated by Imaris (Pearson r = 0.95, p < 0.0001, n = 1822, log transformed data). Volumes for the pre- and postsynaptic puncta were only included when puncta for both pre- and postsynaptic proteins were present to form a full synapse. In some cases, Imaris failed to properly distinguish two neighboring puncta. In these few cases, the combined surface was deleted. The volumes for the puncta of the opposing synaptic proteins were included in the analysis. The x, y, z coordinates of the center point of the volumes for the nuclei and the pre- and postsynaptic proteins were then exported from Imaris to an Excel file. In addition, the volumes for the included pre- and postsynaptic proteins were exported from Imaris to an Excel file. The data were further processed by custom code written in R (R Core Team, 2018) using the following packages: xlsx (Dragulescu and Arendt, 2018), rmisc (Hope, 2013), rgl (Adler et al., 2018), dplyr (Wickham et al., 2018), and tidyr (Wickham and Henry, 2018).

2.5. Data transformation and pillar-modiolar classification of synapses

In order to compare the volumes obtained from different z-stacks, the volumes were normalized by dividing by the median volume for each synaptic protein for each z-stack to be consistent with previous analyses (Liberman et al., 2011).

To assess correlations between presynaptic ribbon volume and postsynaptic protein volume for individual synapses, the pre- and postsynaptic volumes were paired by allocating the closest combination of a presynaptic ribbon and a postsynaptic element a pair ID. To pair (colocalize) volumes, the 3D Euclidean distances between all pre- and postsynaptic volumes were calculated, and the combinations of pre- and postsynaptic volumes with the smallest distance were classified as a pair. The mean distance between the center points of all pairs of pre- and postsynaptic volumes (N = 30 136) was 0.36 μm. A distance of >1 μm was used as the cut-off value to exclude paired synaptic markers. We assumed that paired synaptic markers with larger values were either non-functional or formed from orphan synaptic components where only the pre- or postsynaptic element of a synapse was assigned a volume in Imaris. These paired synaptic markers (≈3% of the synaptic marker pairs) were therefore excluded (Table 2).

The (paired) volumes were then classified as pillar or modiolar by defining a central axis that divided the inner hair cells into pillar and modiolar segments. To define this central axis, a plane was plotted through the row of approximately ten inner hair cells within a stack. To plot this plane, the scalar plane equation was calculated from three points. To determine these three points, two lines were fitted. The first line was fitted to the x, y, z coordinates of the center points for the volumes of the inner hair cell nuclei. The second line was fitted to the x, y, z coordinates of the center points for the volumes of the synaptic proteins. Subsequently, the first point was defined as the x, y, z coordinates of the center point of the fitted line through the volumes of the nuclei. The second and third point were defined as the x, y, z coordinates of the starting and end point of the fitted line through the volumes of the synaptic proteins. A normal vector to the plane was then obtained by taking the cross-product of these two vectors between these three points. The normal vector and the x, y, z coordinates of one of the chosen points were then used to solve for the scalar plane equation. The plane was then calculated and used to classify all (paired) volumes on the pillar side of this plane as “pillar” volumes and all volumes on the modiolar side of this plane as “modiolar” volumes. The normalized sizes of the volumes for the synaptic proteins were then exported from R for statistical analysis in GraphPad (GraphPad Prism version 7.00 for Windows, GraphPad Software, La Jolla California USA) alongside the “pillar” or “modiolar” classification and synaptic pair (paired “CTBP2” and “GluA2”) classification.

2.6. Statistics

Because the distributions of synaptic volumes were skewed, medians rather than means were used as a measure of central tendency. Because the data were not normally distributed, comparisons between pillar and modiolar volumes were performed using the Mann-Whitney *U* test and corrected for multiple comparisons across frequencies using the Bonferroni correction. Correlations were calculated using the Spearman rank test. Analyses were performed in GraphPad.

3. Results

3.1. Volume differences between pillar and modiolar synaptic elements in CBA/CaJ mice

To verify that we could replicate previously shown volume differences in CBA/CaJ mice, we analyzed the volumes for CTBP2 and GluA2 immunopuncta on the pillar and modiolar side in CBA/CaJ mice. Immunolabeling for CTBP2 and GluA2 was punctate and could clearly be detected in CBA/CaJ mice (Fig. 2A–B). After obtaining volumes for these puncta, we compared the distributions of the volumes (normalized as described in section 2.5) between synaptic structures on the pillar and modiolar side of the inner hair cells for both CTBP2 (Fig. 2C) and GluA2 (Fig. 2D), to compare with a previous report of volume distributions for CBA/CaJ mice (Liberman et al., 2011). Our volumes were distributed between ≈0% and ≈300% of the stack median for CTBP2 volumes and between ≈0% and ≈200% for GluA2 volumes, indicating our distributions were narrower than previously reported. To facilitate comparison of our distributions to the original findings (Liberman et al., 2011), we analyzed the mean volumes of these distributions. The mean CTBP2 volume was ≈15% larger on the modiolar side (mean ± sem = 1.18 ± 0.02) compared to the pillar side (mean ± sem = 1.04 ± 0.02, inset Fig. 2C). The mean GluA2 volume size was ≈10% larger on the pillar side (mean ± sem = 1.05 ± 0.01) compared to the modiolar side (mean ± sem = 0.92 ± 0.01, inset Fig. 2D). The previous study found differences of ≈64% for glutamate receptor patches and ≈80% for synaptic ribbons (Liberman et al., 2011). When analyzed separately for the three different frequencies (8, 16, and 32 kHz), the CTBP2 volume was larger on the modiolar side at the 8 and 16 kHz frequency regions (p < 0.0001) but not at the 32 kHz frequency region (Fig. 2E). The GluA2 volumes were smaller on the modiolar side (p < 0.001) for all frequency regions (Fig. 2F). Thus, we observed similar patterns in the presynaptic CTBP2 and postsynaptic GluA2 volumes and specifically the opposing gradients in these volumes as reported previously in CBA/CaJ mice (Liberman et al., 2011).

3.2. Correlations between paired synaptic elements at individual synapses in CBA/CaJ mice

To investigate whether ribbon volume was inversely correlated to glutamate receptor patch volume for paired elements of individual synapses, we further studied correlations between paired CTBP2 and GluA2 volumes pooled over all frequency regions. We found inverse correlations between CTBP2 and GluA2 volumes (Fig. 2G–H) for synapses located on both the pillar (ρ = −0.09, p = 0.002, n = 1018 pairs) and modiolar side of the inner hair cell (ρ = −0.08, p = 0.004, n = 1114 pairs).

To quantify how many synapses adhered to the predicted pattern of smaller ribbons with larger glutamate receptors on the pillar side and vice versa on the modiolar side, we divided all paired

Table 2
R script classification of all pre- and postsynaptic markers in all three strains for all normalized volumes[n] and subgroups of volumes that are part of synaptic volume pairs[s].

		CTBP2		GluA2		Shank1a		Homer		PSD95	
Individual volumes		Pillar	Modiolar	Pillar	Modiolar	Pillar	Modiolar	Pillar	Modiolar	Pillar	Modiolar
CBA/CaJ	N synapses	1085	1249	998	1225	–	–	–	–	–	–
	Percentage	46.5	53.5	44.9	55.1	–	–	–	–	–	–
	Median	0.94	1.08	1.05	0.92	–	–	–	–	–	–
FVB/NJ	N synapses	3564	3769	1052	1121	734	744	1086	1211	607	693
	Percentage	48.6	51.4	48.4	51.6	49.7	50.3	47.3	52.7	46.7	53.3
	Median	0.96	1.05	0.87	0.95	0.95	1.08	0.97	1.03	0.86	1.09
C57BL/6	N synapses	2221	2256	698	700	669	720	760	796	1451	1507
	Percentage	49.6	50.4	49.6	50.4	48.2	51.8	48.8	51.2	49.1	50.9
	Median	0.97	1.03	0.99	1.01	0.96	1.04	0.89	1.11	0.96	1.05
Paired volumes											
CBA/CaJ	N synapses	1018	1114	1018	1114	–	–	–	–	–	–
	Percentage	48	52	48	52	–	–	–	–	–	–
	Median	0.94	1.06	1.08	0.93	–	–	–	–	–	–
FVB/NJ	N synapses	3372	3585	1013	1076	723	712	1079	1173	557	624
	Percentage	48	52	48	52	50	50	48	52	47	53
	Median	0.97	1.05	0.98	1.02	0.95	1.10	0.97	1.03	0.87	1.10
C57BL/6	N synapses	3525	3555	651	646	656	701	774	756	1444	1452
	Percentage	50	50	50	50	48	52	51	49	50	50
	Median	0.97	1.03	0.99	1.02	0.96	1.04	0.90	1.11	0.96	1.06

[n] = All sizes of volumes were normalized to the median size for each protein for each stack independently.
[s] = Volumes were classified as belonging to a synaptic pair when both a pre- and post synaptic element were juxtaposed within 1 μm of each other (97% of volumes).

volumes over four quadrants of a scatterplot (Fig. 2G–H). The first quadrant (Q1) contained paired volumes for which CTBP2 and GluA2 volumes were both larger than 1. The second quadrant (Q2) contained paired volumes for which CTBP2 volumes were smaller than 1 and GluA2 volumes were larger than 1. The third quadrant (Q3) contained paired volumes for which CTBP2 and GluA2 volumes were both smaller than 1. The fourth quadrant (Q4) contained paired volumes for which CTBP2 volumes were larger than 1 and GluA2 volumes were smaller than 1. We quantified the fraction of paired volumes in each of these quadrants separately for paired volumes on the pillar side and on the modiolar side. Larger fractions of paired volumes in Q2 on the pillar side and Q4 on the modiolar side would be consistent with an inverse correlation. In contrast, larger fractions of paired volumes in Q3 on the pillar side and Q1 on the modiolar side would be consistent with a positive correlation. Consistent with observations of opposing volume gradients at the population levels, the largest fraction of paired volumes on the pillar side was in Q2, and the largest fraction of paired volumes on the modiolar side was in Q4.

These findings confirm that our methodological approach can detect opposing volume gradients in CBA/CaJ mice and substantiate previous findings in CBA/CaJ mice (Liberman et al., 2011). Furthermore, we observed the implied inverse correlation for volumes of the paired synaptic elements at individual synapses.

3.3. Volume differences between pillar and modiolar synaptic elements in C57BL/6 and FVB/NJ mice

To examine whether opposing volume gradients in presynaptic CTBP2 and postsynaptic GluA2 were present in other mouse strains, we examined volume differences in C57BL/6 and FVB/NJ mice. For C57BL/6 mice, CTBP2 (Fig. 3A) and GluA2 (Fig. 3B) puncta were clearly immunolabeled, similar to CBA/CaJ mice. We again compared pillar and modiolar CTBP2 and GluA2 volumes at three different cochlear frequency regions (8, 16, and 32 kHz). The CTBP2 volumes were larger on the modiolar side than on the pillar side ($p < 0.05$) at all cochlear frequencies (Fig. 3C). However, there were no differences in the GluA2 volumes between the pillar and modiolar side at any cochlear frequency region (Fig. 3D).

In FVB/NJ mice, CTBP2 (Fig. 4A) and GluA2 (Fig. 4B) puncta were clearly immunolabeled, similar to observations in CBA/CaJ and C57BL/6 mice. Again, we compared pillar and modiolar CTBP2 and GluA2 volumes at three different cochlear frequency regions (8, 16, and 32 kHz). The CTBP2 volumes were larger on the modiolar side than on the pillar side for both the 8 and 16 kHz region ($p < 0.0001$) but not different for the 32 kHz region (Fig. 4C). The GluA2 volumes were larger on the modiolar than on the pillar side for both the 8 and 16 kHz region ($p < 0.005$) but not different for the 32 kHz region (Fig. 4D). Thus, for both C57BL/6 and FVB/NJ mice, presynaptic CTBP2 volumes were generally larger on the modiolar side across most frequencies. In contrast, GluA2 volumes were either not different between the pillar and modiolar side or larger on the modiolar side, indicating concurrent volume gradients.

3.4. Correlations between paired synaptic elements at individual synapses in C57BL/6 and FVB/NJ mice

To investigate whether ribbon volume was inversely correlated to glutamate receptor patch volume for paired elements of individual synapses in C57BL/6 and FVB/NJ mice, we further studied correlations between paired CTBP2 and GluA2 volumes pooled over all frequency regions. In C57BL/6 mice, we found a positive correlation between CTBP2 volumes and GluA2 volumes (Fig. 3E–F), for synapses located on both the pillar ($\rho = 0.21$) and the modiolar side ($\rho = 0.20$). We also found a positive correlation between CTBP2 volumes and GluA2 volumes in FVB/NJ mice (Fig. 4E–F), for synapses located on both the pillar ($\rho = 0.21$) and the modiolar side ($\rho = 0.20$). These correlations suggest that relatively small ribbons juxtapose relatively small glutamate receptor patches in synapses on the pillar side and both ribbons and glutamate receptor patches are larger in synapses on the modiolar side. To quantify the proportion of synapses that adhered to this pattern, we again assigned the paired volumes to one of four quadrants (as described in section 3.2). In both C57BL/6 and FVB/NJ mice, the largest fractions of paired volumes were present in Q3 on the pillar side and in Q1 on the modiolar side. Thus, in both strains of mice, quadrant analysis substantiated the positive correlations. However, only between 30% and 40% of all synapses were found in the expected quadrants.

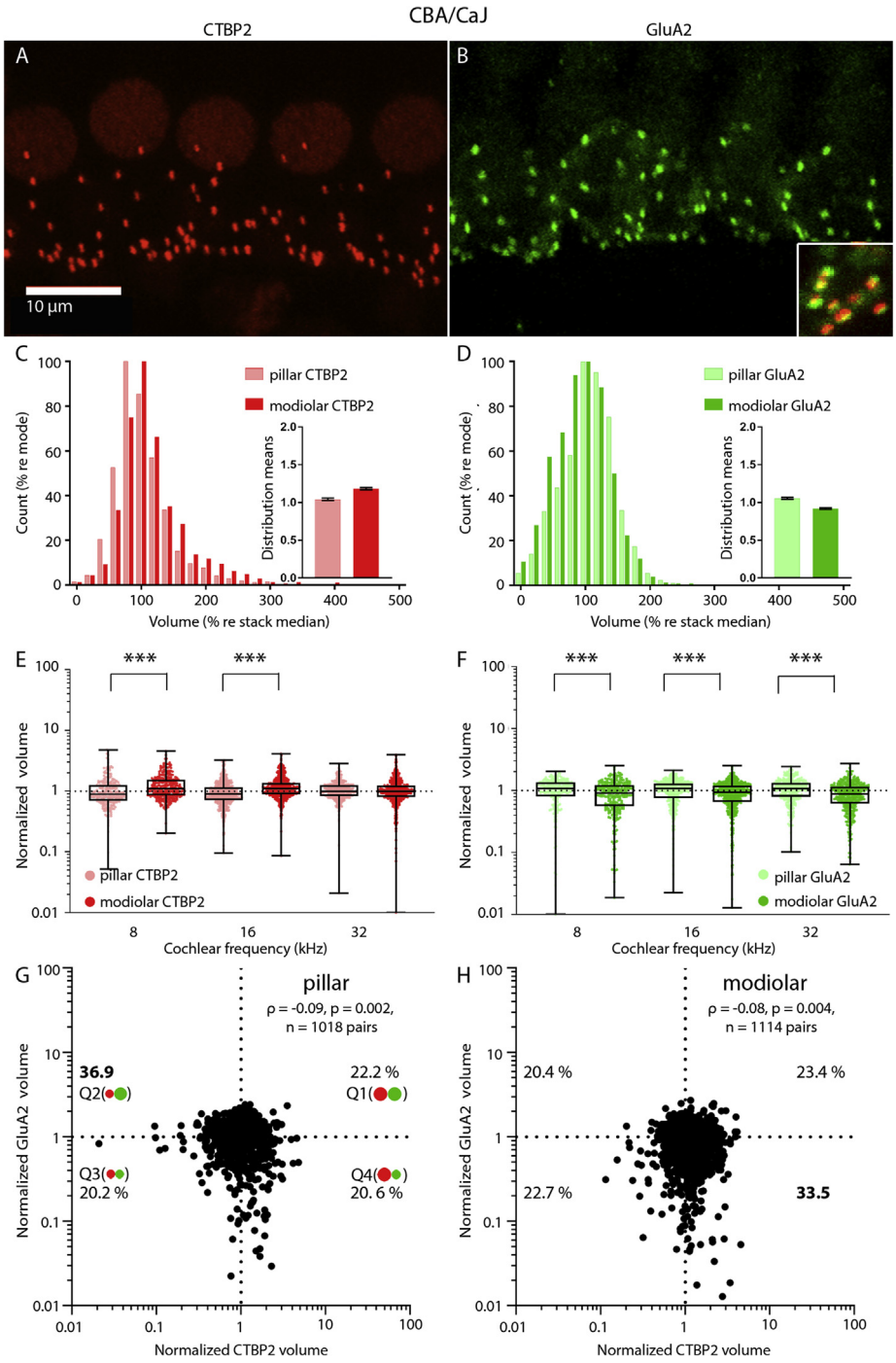

Fig. 2. Comparison of the CTBP2 and GluA2 volumes between pillar and modiolar synapses in CBA/CaJ mice. To compare presynaptic CTBP2 and postsynaptic GluA2 volumes among pillar and modiolar synapses, the volume distributions and volume as a function of frequency/tonotopic region was examined in CBA/CaJ mice. **A-B)** Micrographs of immunolabeled presynaptic CTBP2-positive ribbons (A) and postsynaptic GluA2-containing receptor patches (B). Scale bar in A applies to both panels. Inset depicts the merged micrographs. **C-D)** Distributions of the normalized CTBP2 (C) and GluA2 (D) volumes for pillar and modiolar synapses. Insets indicate the means for each subgroup. These volume distributions and means are plotted similar to a previous study to facilitate comparison (Liberman et al., 2011). **E-F)** Boxplots showing the normalized CTBP2 (E) and GluA2 (F) volumes over the three frequency regions examined. Boxplots indicate the 25th and 75th percentile around the median with the individual datapoints overlaid. Whiskers extend from the minimum to the maximum. Significant differences are indicated by * = $p < 0.05$, ** = $p < 0.01$, *** = $p < 0.001$. **G-H)** Scatterplots of the paired normalized volumes of presynaptic CTBP2 on the x-axis and postsynaptic GluA2 on the y-axis from individual synapses on the pillar (G) and modiolar (H) side.

3.5. Volume differences in postsynaptic density proteins in C57BL/6 and FVB/NJ mice

To investigate if opposing volume gradients for other proteins of the postsynaptic density were detectable, we repeated our volume gradient analysis in C57BL/6 and FVB/NJ mice for three additional postsynaptic density proteins: Shank1, Homer, and PSD95. All three of these proteins are part of the postsynaptic density that contains the GluA2 subunit (Sheng and Hoogenraad, 2007). In C57BL/6 mice, Shank1 (Fig. 5A), Homer (Fig. 5B), and PSD95 (Fig. 5C)

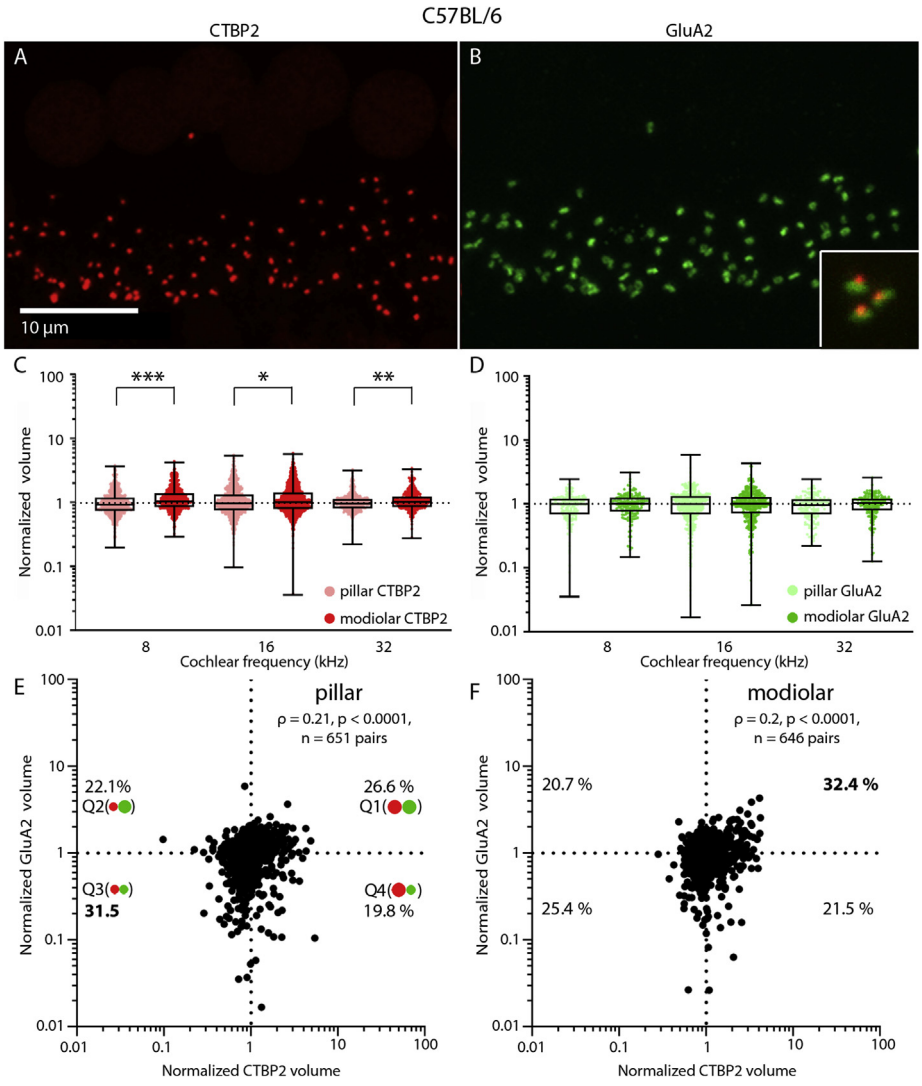

Fig. 3. Comparison of the CTBP2 and GluA2 volumes between pillar and modiolar synapses in C57BL/6 mice. To compare presynaptic CTBP2 and postsynaptic GluA2 volumes among pillar and modiolar synapses, the volume distributions and volume as a function of frequency/tonotopic region was examined in C57BL/6 mice. **A-B)** Micrographs of immunolabeled presynaptic CTBP2-positive ribbons (A) and postsynaptic GluA2-containing receptor patches (B). Scale bar in A applies to both panels. Inset depicts the merged micrographs. **C-D)** Boxplots showing the normalized CTBP2 (C) and GluA2 (D) volumes over the three frequency regions examined. Boxplots indicate the 25th and 75th percentile around the median with the individual datapoints overlaid. Whiskers extend from the minimum to the maximum. Significant differences are indicated by * = $p < 0.05$, ** = $p < 0.01$, *** = $p < 0.001$. **E-F)** Scatterplots of the paired normalized volumes of presynaptic CTBP2 on the x-axis and postsynaptic GluA2 on the y-axis from individual synapses located on the pillar (E) or modiolar (F) side.

immunopuncta were clearly visible, similar to the GluA2 immunopuncta. Shank1 volumes were larger on the modiolar side than on the pillar side at the 8 kHz region ($p < 0.0005$) but smaller on the modiolar side than on the pillar side at the 16 kHz region ($p < 0.0005$). No differences were detectable between volumes on the modiolar and pillar sides at the 32 kHz region (Fig. 5D). Homer volumes were larger on the modiolar side than on the pillar side ($p < 0.0001$) at all cochlear frequency regions (Fig. 5E). PSD95 volumes were larger on the modiolar side than on the pillar side ($p < 0.0001$) at the 8 and 32 kHz regions (Fig. 5F) but not different at the 16 kHz region. In FVB/NJ mice, Shank1 (Fig. 6A), Homer (Fig. 6B), and PSD95 (Fig. 6C) immunopuncta were also clearly visible. Shank1 volumes were larger on the modiolar side than on the pillar side at 32 kHz ($p < 0.0001$) but not significantly different between the modiolar and pillar sides at the other cochlear frequency regions (Fig. 6D). Homer volumes were larger on the modiolar side than on the pillar side at 8 kHz ($p < 0.0005$) but not significantly different between the modiolar and pillar sides at the other cochlear frequency regions (Fig. 6E). Finally, PSD95 volumes were larger on the modiolar side than on the pillar side ($p < 0.005$) at all cochlear frequencies (Fig. 6F).

These results are similar to the results for the GluA2 volumes in C57BL/6 and FVB/NJ mice, where we found either no detectable postsynaptic volume gradient or a volume gradient that is concurrent to the CTBP2 volume gradient. Furthermore, across the strains and frequencies, PSD95 volumes showed the most consistent concurrent volume gradient of the four postsynaptic proteins studied.

3.6. Correlations between paired synaptic elements at individual synapses in C57BL/6 and FVB/NJ mice

We further investigated whether an inverse or positive correlation could be found between presynaptic CTBP2 and either Shank1, Homer, or PSD95 for paired elements of individual synapses by calculating the correlation between the paired volumes of

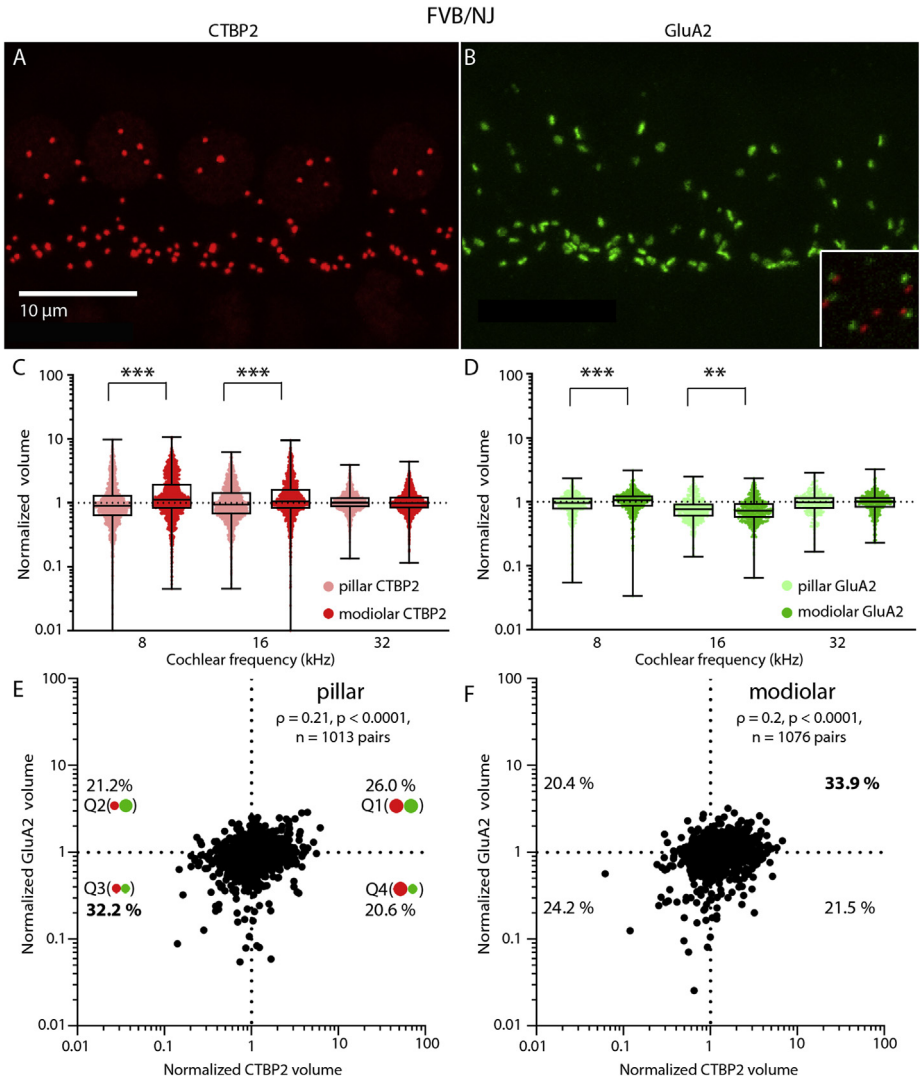

Fig. 4. Comparison of the CTBP2 and GluA2 volumes between pillar and modiolar synapses in FVB/NJ mice. To compare presynaptic CTBP2 and postsynaptic GluA2 volumes among pillar and modiolar synapses, the volume distributions and volume as a function of frequency/tonotopic region was examined in FVB/NJ mice. **A-B)** Micrographs of immunolabeled presynaptic CTBP2-positive ribbons (A) and postsynaptic GluA2-containing receptor patches (B). Scale bar in A applies to both panels. Inset depicts the merged micrographs. **C-D)** Boxplots showing the normalized CTBP2 (C) and GluA2 (D) volumes over the three frequency regions examined. Boxplots indicate the 25th and 75th percentile around the median with the individual datapoints overlaid. Whiskers extend from the minimum to the maximum. Significant differences are indicated by * = $p < 0.05$, ** = $p < 0.01$, *** = $p < 0.001$. **E-F)** Scatterplots of the paired normalized volumes of presynaptic CTBP2 on the x-axis and postsynaptic GluA2 on the y-axis from individual synapses located on the pillar (E) or modiolar (F) side.

the respective postsynaptic density protein and presynaptic CTBP2. We found positive correlations for paired volumes between CTBP2 and Shank1, Homer, and PSD95 in both C57BL/6 and FVB/NJ mice (Figs. 5 and 6 G-L). We also examined the partitioning of paired volumes into separate quadrants (see section 3.2). In C57BL/6 mice, the largest fractions of paired volumes for Shank1 and Homer were present in Q3 (Fig. 5G–H) on the pillar side and in Q1 (Fig. 5J–K) on the modiolar side. The largest fractions of paired volumes for PSD95 were present in Q2 (Fig. 5I) on the pillar side and in Q1 (Fig. 5L) on the modiolar side. In FVB/NJ mice, the largest fractions of paired volumes for Shank1, Homer, and PSD95 were present in Q3 (Fig. 6G–I) on the pillar side and in Q1 (Fig. 6J-L) on the modiolar side.

In conclusion, volume gradients in Shank1, Homer, and PSD95 in C57BL/6 and FVB/NJ mice were similar to the volume gradients observed for GluA2 in these strains. Specifically, for all postsynaptic proteins, the volumes were either indicative of no volume gradient or a volume gradient concurrent to the CTBP2 volume gradient. These results were further supported when analyzing correlations between the volumes of paired synaptic partners at individual synapses, which showed consistent positive correlations between presynaptic CTBP2 and all postsynaptic proteins evaluated, i.e., Shank1, Homer, and PSD95.

4. Discussion

The main aim of this study was to examine whether opposing volume gradients of CTBP2 and GluA2 that were previously observed in CBA/CaJ mice are also observed in C57BL/6, and FVB/NJ mice. We found volume gradients in presynaptic CTBP2 consistently in all three strains of mice and consistently across different cochlear frequencies, including 8, 16, and 32 kHz. Specifically, CTBP2 volumes were larger in synapses on the modiolar side than for synapses on the pillar side in all three strains of mice. In contrast, we did not find consistently expressed postsynaptic volume gradients across the three strains. In CBA/CaJ mice, we found

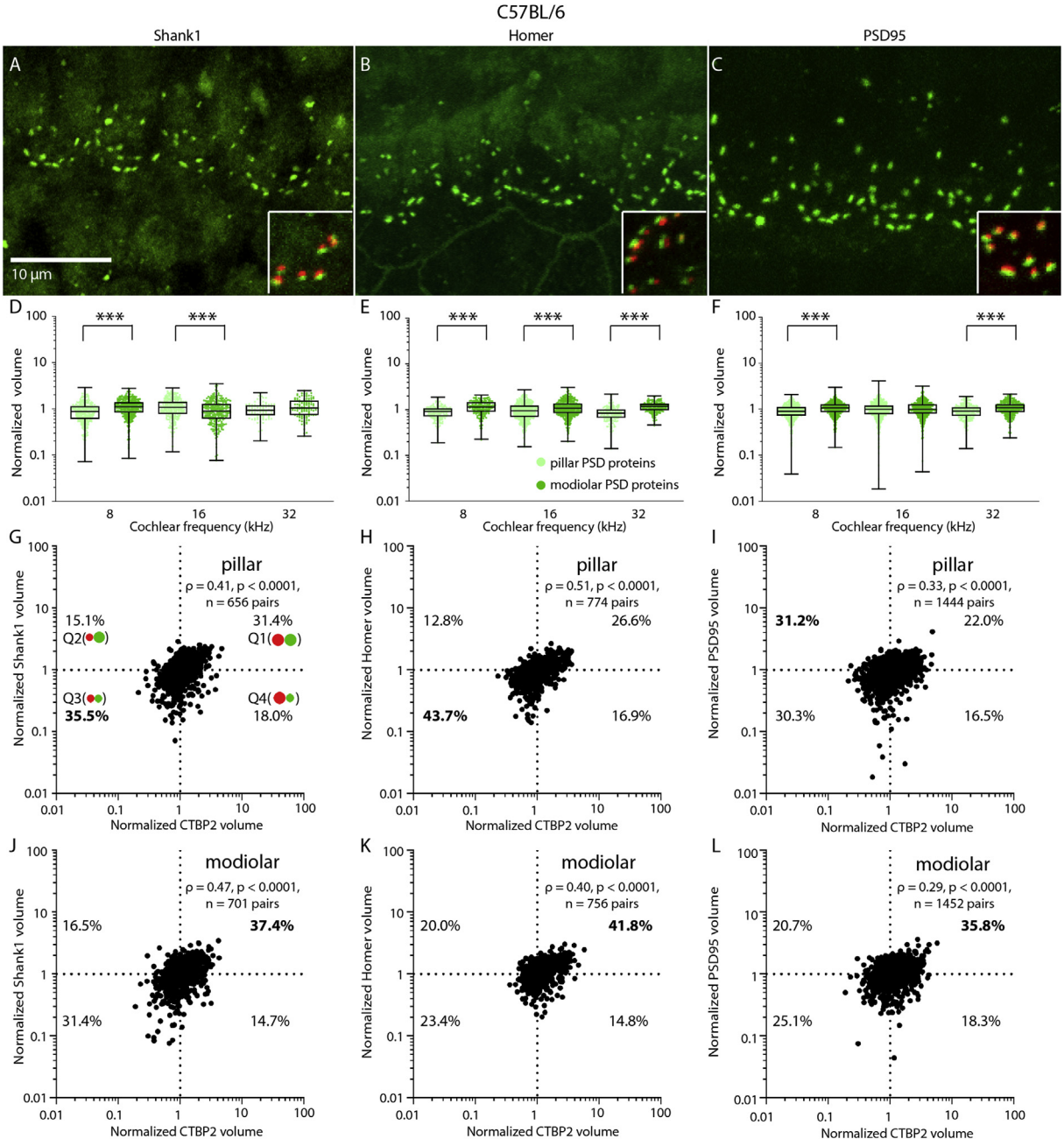

Fig. 5. Comparison of the Shank1, Homer, and PSD95 volumes between pillar and modiolar synapses in C57BL/6 mice. To compare presynaptic CTBP2 and postsynaptic Shank1, Homer, and PSD95 volumes among pillar and modiolar synapses, the volume distributions and volume as a function of frequency/tonotopic region was examined in C57BL/6 mice. **A-C)** Micrographs of immunolabeled postsynaptic Shank1 (A), Homer (B), and PSD95 (C). Scale bar in A applies to all panels. Insets depict the merged micrographs. **D-F)** Boxplots showing the normalized Shank1 (D), Homer (E), and PSD95 (F) volumes over the three frequency regions examined. Boxplots indicate the 25th and 75th percentile around the median with the individual datapoints overlaid. Whiskers extend from the minimum to the maximum. Significant differences are indicated by * = $p < 0.05$, ** = $p < 0.01$, *** = $p < 0.001$. **G-L)** Scatterplots of the paired normalized volumes of presynaptic CTBP2 on the x-axis and either postsynaptic Shank1, Homer, or PSD95 on the y-axis from individual synapses located on the pillar (G–I) or modiolar (J–L) side.

smaller GluA2 volumes in auditory nerve fibers contacting the modiolar side than in fibers contacting the pillar side. In C57BL/6 and FVB/NJ mice, we found no consistent difference in GluA2 volume between auditory nerve fibers contacting the modiolar side and those contacting the pillar side. For three additional postsynaptic density proteins (Shank1, Homer, and PSD95), we found that the protein volumes were generally larger in auditory nerve fibers contacting the modiolar compared to pillar side in C57BL/6 and FVB/NJ mice. Together, these findings indicate opposing pre- and postsynaptic volume gradients in CBA/CaJ mice and, in contrast, concurrent pre- and postsynaptic volume gradients in C57BL/6 and FVB/NJ mice. Importantly, the direction of these volume gradients determined for the population of presynaptic ribbons and various postsynaptic proteins were always consistent with the correlations between volumes of paired pre- and postsynaptic elements for individual synapses. In fact, the correlations at the level of individual synapses were more consistent than the gradients across the pillar-modiolar axis of a larger sample of inner hair cells. This observation suggests that synaptic morphology does vary systematically between individual synapses but that different

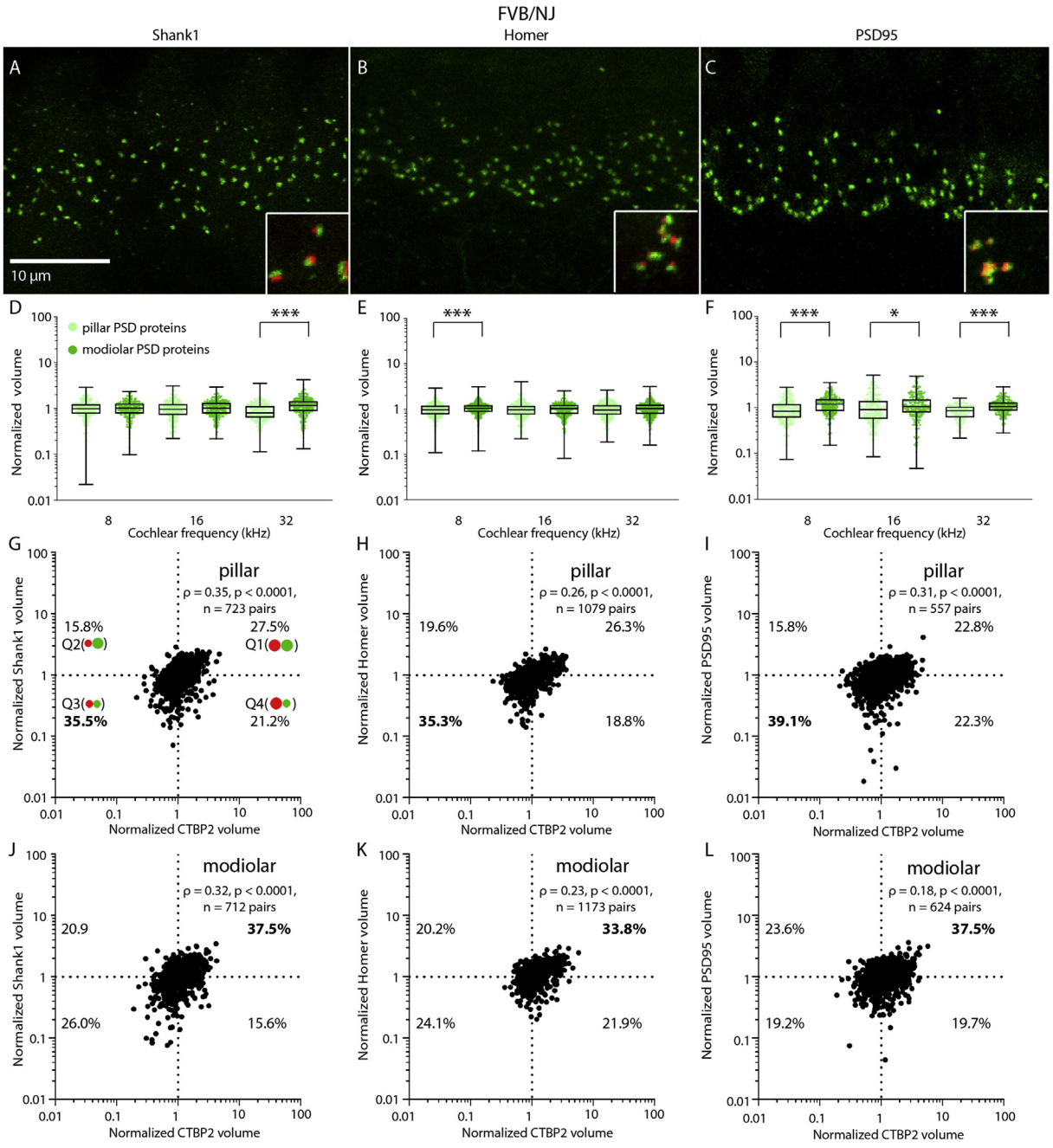

Fig. 6. Comparison of the Shank1, Homer, and PSD95 volumes between pillar and modiolar synapses in FVB/NJ mice. To compare presynaptic CTBP2 and postsynaptic Shank1, Homer, and PSD95 volumes among pillar and modiolar synapses, the volume distributions and volume as a function of frequency/tonotopic region was examined in FVB/NJ mice. **A-C)** Micrographs of immunolabeled postsynaptic Shank1 (A), Homer (B), and PSD95 (C). Scale bar in A applies to all panels. Insets depict the merged micrographs. **D-F)** Boxplots showing the normalized Shank1 (D), Homer (E), and PSD95 (F) volumes over the three frequency regions examined. Boxplots indicate the 25th and 75th percentile around the median with the individual datapoints overlaid. Whiskers extend from the minimum to the maximum. Significant differences are indicated by * = $p < 0.05$, ** = $p < 0.01$, *** = $p < 0.001$. **G-L)** Scatterplots of the paired normalized volumes of presynaptic CTBP2 on the x-axis and either postsynaptic Shank1, Homer, or PSD95 on the y-axis from individual synapses located on the pillar (G–I) or modiolar (J–L) side.

morphologies do not always clearly segregate spatially.

4.1. Opposing versus concurrent synaptic volume gradients in mice

Our observations of opposing gradients in the volumes of pre- and postsynaptic elements along the pillar-modiolar axis in CBA/CaJ mice is consistent with previous reports (Liberman et al., 2011; Liberman and Liberman, 2016; Yin et al., 2014). In addition, we show here inverse correlations between the volumes of paired synaptic partners at individual synapses that are implied by the observation of opposing gradients. However, we observed only a subgroup of around 30–40% of all individual synapses on both the pillar and modiolar side with paired pre- and postsynaptic volumes corresponding to the expectations from the opposing population gradients (Fig. 2G–H, pillar Q2, modiolar Q4). In addition, the overall distribution of pre- and postsynaptic volumes on both the pillar and modiolar side was much narrower in our work (≈0–300% relative to the stack median, Fig. 2C–D) compared to

previous work (≈0–800% relative to the stack median, (Liberman et al., 2011; Liberman and Liberman, 2016; Yin et al., 2014). This difference likely contributed to the smaller differences in synaptic protein volumes between the pillar and modiolar sides and thus smaller opposing gradients (Fig. 2E–F) observed in our study compared to previous work (Liberman et al., 2011). These findings of narrower distributions of pre- and postsynaptic protein volumes on both the pillar and modiolar side, smaller differences in synaptic protein volumes between the pillar and modiolar sides, and correspondingly smaller gradients were also observed in C57BL/6 and FVB/NJ mice (data not shown). Mice were of a similar age as described in the original study in mice (Liberman et al., 2011), and thus variation in age likely did not have an effect on these discrepancies between studies. Although the narrower distributions of pre- and postsynaptic volumes on both the pillar and modiolar side could potentially reduce the ability to detect synaptic volume gradients and especially the postsynaptic volume gradients, which have been reported to be smaller than the presynaptic volume gradients (Liberman et al., 2011), we nevertheless replicated previously reported synaptic volume gradients in CBA/CaJ mice. Furthermore, in C57BL/6 and FVB/NJ mice, results were generally consistent between all four postsynaptic proteins examined: if volume gradients were present, then these gradients were concurrent to the presynaptic volume gradient.

In some cases, specifically for the C57BL/6 GluA2 analysis, no statistically significant volume gradient between pillar and modiolar locations could be detected. However, volume gradients were observed for the other three PSD proteins (Shank1, Homer, and PSD95). Furthermore, within individual synapses, correlations with presynaptic ribbon volume were observed for all postsynaptic protein volumes evaluated and for both C57BL/6 and FVB/NJ mice. Together, these observations suggest that gradients of the volumes of presynaptic ribbons and other PSD proteins (Shank1, Homer, and PSD95) were, as a rule, concurrent in the C57BL/6 mice. In C57BL/6 and FVB/NJ mice, volume gradients for particular synaptic elements have not been studied previously and, thus, we cannot make direct comparisons. However, in FVB/NJ mice, studies examining changes in the volumes of paired pre- and postsynaptic elements in FOXO3-KO mice or after noise exposure reported an inverse correlation between volumes, based on scatterplots of the raw fluorescent volumes (Gilels et al., 2013; Paquette et al., 2016). Unfortunately, the authors did not probe the spatial segregation along the pillar-modiolar axis in FVB/NJ mice. Additional postsynaptic density proteins besides GluA2 have not been studied in CBA/CaJ mice. Future studies should examine whether the opposing gradient found for GluA2 is consistent across other postsynaptic density proteins.

4.2. Opposing versus concurrent synaptic volume gradients in mammals

Our observations in these three mouse strains, together with work in other rodents and in cat, suggest that an opposing volume gradient may not be the most representative organization of the synapses between the inner hair cells and the auditory nerve fibers. In cat, volume differences in presynaptic ribbon structures between terminals of high-spontaneous-rate fibers on the pillar side of inner hair cells and terminals of low- and medium-spontaneous rate fibers on the modiolar side, were observed, but the postsynaptic terminals themselves were reported to be of equal size (Merchan-Perez and Liberman, 1996). In guinea pig, no volume gradient for postsynaptic glutamate receptor patches could be detected (Furman et al., 2013). Moreover, in gerbil, postsynaptic volume gradients were reported that were concurrent to the presynaptic CTBP2 volume gradient (Zhang et al., 2018). Thus, pre-synaptic ribbon gradients and concurrent, rather than opposing, postsynaptic gradients may be a more typical feature of organization of the synapses between the inner hair cells and the auditory nerve fibers.

4.3. Implications

These observations have important implications when considering the contribution of the morphology of synapses between the inner hair cells and the auditory nerve fibers to the physiological properties of the auditory neurons. First, on one hand, we found that correlations between the volumes of paired pre- and postsynaptic elements for individual synapses follow expectations from gradients across the population of synapses. This finding suggests that differences in synaptic morphology could indeed contribute to differences in the physiology of individual auditory nerve fibers. On the other hand, we found that the variance of volume measurements is high, the correlations between pre- and postsynaptic volumes are weak, and the spatial segregation of ribbon and glutamate receptor patch volumes along the pillar-modiolar axis tends to be even weaker (and sometimes not detectable) even for large samples. Thus, further examination is necessary to determine the extent to which the morphology of auditory nerve fiber synapses contributes to the physiological properties of the fibers themselves.

Second, the implication that concurrent volume gradients may be more typical across mammals suggests that the low spontaneous rate auditory nerve fibers, which are thought to face larger ribbons, also have larger glutamate receptor patches. As the glutamate receptors are thought to be key players in mediating excitotoxic auditory nerve fiber damage (Chen et al., 2009, 2007), larger glutamate receptor patches could, in fact, be more consistent with their reportedly increased vulnerability to damage (Furman et al., 2013).

Third, the variability of postsynaptic volume gradients across mouse strains indicates that there are additional factors contributing to auditory nerve fiber thresholds and spontaneous activity. Presynaptically, this activity may depend on vesicular release rate (Frank et al., 2009; Ohn et al., 2016) or heterogeneity in monophasic versus multiphasic spontaneous excitatory postsynaptic currents (Grant et al., 2010). Postsynaptically, the lateral efferent system has been shown to affect synaptic volume gradients (Yin et al., 2014) and may contribute to the determination of firing rates in additional ways.

Fourth, other factors are also known or expected to contribute to variations in the spontaneous firing of auditory nerve fibers. For example, auditory nerve fiber excitability is regulated by the expression and proper localization of ion channels (Davis and Crozier, 2015; Kim and Rutherford, 2016; Oak and Yi, 2014; Reijntjes et al., 2019; Reijntjes and Pyott, 2016). Modelling experiments reproduce many aspects of the variation in spontaneous firing of auditory nerve fibers simply by varying the rates of vesicle depletion (Peterson and Heil, 2018). Further work will be necessary to determine how variations in ion channel expression, vesicle dynamics (and other factors) in concert with morphological organization of the of pre- and postsynaptic elements causally contribute to the spontaneous activity of individual auditory nerve fibers.

Funding

This work was supported by grants from the University of Groningen and the Heinsius Houbolt Foundation to S.J.P.

Declaration of competing interest

The authors declare that the research was conducted in the absence of any commercial or financial relationships that could be construed as a potential conflict of interest.

Acknowledgements

D.O.J.R. designed research, acquired data, analyzed data, and contributed to writing the paper; C.K. designed research and contributed to data analysis and writing the paper, S.J.P designed research and contributed to data analysis and writing the paper. We thank Prof. Georg Klump (Carl von Ossietzky University Oldenburg) for providing CBA/CaJ mice.

Appendix A. Supplementary data

Supplementary data to this article can be found online at https://doi.org/10.1016/j.heares.2020.107933.

References

Adler, D., Murdoch, D., others, 2018. Rgl: 3D Visualization Using OpenGL.
Barbary, A. El, 1991. Auditory nerve of the normal and jaundiced rat. I. Spontaneous discharge rate and cochlear nerve histology. Hear. Res. https://doi.org/10.1016/0378-5955(91)90138-Y.
Barone, C.M., Douma, S., Reijntjes, D.O.J., Browe, B.M., Köppl, C., Klump, G., Park, T.J., Pyott, S.J., 2019. Altered cochlear innervation in developing and mature naked and Damaraland mole rats. J. Comp. Neurol. https://doi.org/10.1002/cne.24682.
Borg, E., Engström, B., Linde, G., Marklund, K., 1988. Eighth nerve fiber firing features in normal-hearing rabbits. Hear. Res. https://doi.org/10.1016/0378-5955(88)90061-5.
Chen, Z., Kujawa, S.G., Sewell, W.F., 2007. Auditory sensitivity regulation via rapid changes in expression of surface AMPA receptors. Nat. Neurosci. https://doi.org/10.1038/nn1974.
Chen, Z., Peppi, M., Kujawa, S.G., Sewell, W.F., 2009. Regulated expression of surface AMPA receptors reduces excitotoxicity in auditory neurons. J. Neurophysiol. 102, 1152–1159. https://doi.org/10.1152/jn.00288.2009.
Davis, R.L., Crozier, R.A., 2015. Dynamic firing properties of type I spiral ganglion neurons. Cell Tissue Res. https://doi.org/10.1007/s00441-014-2071-x.
Dragulescu, A.A., Arendt, C., 2018. Xlsx: Read, Write, Format Excel 2007 and Excel 97/2000/XP/2003 Files.
Frank, T., Khimich, D., Neef, A., Moser, T., 2009. Mechanisms contributing to synaptic Ca2+ signals and their heterogeneity in hair cells. Proc. Natl. Acad. Sci. https://doi.org/10.1073/pnas.0813213106.
Furman, A.C., Kujawa, S.G., Liberman, M.C., 2013. Noise-induced cochlear neuropathy is selective for fibers with low spontaneous rates. J. Neurophysiol. https://doi.org/10.1152/jn.00164.2013.
Gilels, F., Paquette, S.T., Zhang, J., Rahman, I., White, P.M., 2013. Mutation of Foxo3 causes adult onset auditory neuropathy and alters cochlear synapse architecture in mice. J. Neurosci. https://doi.org/10.1523/jneurosci.2529-13.2013.
Glowatzki, E., Fuchs, P.A., 2002. Transmitter release at the hair cell ribbon synapse. Nat. Neurosci. 5, 147–154. https://doi.org/10.1038/nn796.
Grant, L., Yi, E., Glowatzki, E., 2010. Two modes of release shape the postsynaptic response at the inner hair cell ribbon synapse. J. Neurosci. https://doi.org/10.1523/jneurosci.4439-09.2010.
Heil, P., Peterson, A.J., 2015. Basic response properties of auditory nerve fibers: a review. Cell Tissue Res. https://doi.org/10.1007/s00441-015-2177-9.
Hope, R.M., 2013. Rmisc: Rmisc: Ryan Miscellaneous.
Kalluri, R., Monges-Hernandez, M., 2017. Spatial gradients in the size of inner hair cell ribbons emerge before the onset of hearing in rats. JARO J. Assoc. Res. Otolaryngol. https://doi.org/10.1007/s10162-017-0620-1.
Kane, K.L., Longo-Guess, C.M., Gagnon, L.H., Ding, D., Salvi, R.J., Johnson, K.R., 2012. Genetic background effects on age-related hearing loss associated with Cdh23 variants in mice. Hear. Res. https://doi.org/10.1016/j.heares.2011.11.007.
Kim, K.X., Rutherford, M.A., 2016. Maturation of NaV and KV channel topographies in the auditory nerve spike initiator before and after developmental onset of hearing function. J. Neurosci. https://doi.org/10.1523/jneurosci.3437-15.2016.
Kommareddi, P., Nair, T., Kakaraparthi, B.N., Galano, M.M., Miller, D., Laczkovich, I., Thomas, T., Lu, L., Rule, K., Kabara, L., Kanicki, A., Hughes, E.D., Jones, J.M., Hoenerhoff, M., Fisher, S.G., Altschuler, R.A., Dolan, D., Kohrman, D.C., Saunders, T.L., Carey, T.E., 2015. Hair cell loss, spiral ganglion degeneration, and progressive sensorineural hearing loss in mice with targeted deletion of slc44a2/ctl2. JARO J. Assoc. Res. Otolaryngol. https://doi.org/10.1007/s10162-015-0547-3.
Liberman, L.D., Liberman, M.C., 2016. Postnatal maturation of auditory-nerve heterogeneity, as seen in spatial gradients of synapse morphology in the inner hair cell area. Hear. Res. https://doi.org/10.1016/j.heares.2016.06.002.
Liberman, L.D., Wang, H., Liberman, M.C., 2011. Opposing gradients of ribbon size and AMPA receptor expression underlie sensitivity differences among cochlear-nerve/hair-cell synapses. J. Neurosci. 31, 801–808. https://doi.org/10.1523/JNEUROSCI.3389-10.2011.
Liberman, M.C., 1982. Single-neuron labeling in the cat auditory nerve. Science 80. https://doi.org/10.1126/science.7079757.
Liberman, M.C., 1978. Auditory-nerve response from cats raised in a low-noise chamber. J. Acoust. Soc. Am. 63, 442–455. https://doi.org/10.1121/1.381736.
Liberman, M.C., Oliver, M.E., 1984. Morphometry of intracellularly labeled neurons of the auditory nerve: correlations with functional properties. J. Comp. Neurol. https://doi.org/10.1002/cne.902230203.
Merchan-Perez, A., Liberman, M.C., 1996. Ultrastructural differences among afferent synapses on cochlear hair cells: correlations with spontaneous discharge rate. J. Comp. Neurol. https://doi.org/10.1002/(SICI)1096-9861(19960722)371:2<208::AID-CNE2>3.3.CO;2-P.
Meyer, A.C., Moser, T., 2010. Structure and function of cochlear afferent innervation. Curr. Opin. Otolaryngol. Head Neck Surg. https://doi.org/10.1097/MOO.0b013e32833e0586.
Müller, M., Von Hünerbein, K., Hoidis, S., Smolders, J.W.T., 2005. A physiological place-frequency map of the cochlea in the CBA/J mouse. Hear. Res. 202, 63–73. https://doi.org/10.1016/j.heares.2004.08.011.
Oak, M.H., Yi, E., 2014. Voltage-gated K+channels contributing to temporal precision at the inner hair cell-auditory afferent nerve fiber synapses in the mammalian cochlea. Arch Pharm. Res. (Seoul). https://doi.org/10.1007/s12272-014-0411-8.
Ohlemiller, K.K., Echteler, S.M., Siegel, J.H., 2005. Factors that influence rate-versus-intensity relations in single cochlear nerve fibers of the gerbil. J. Acoust. Soc. Am. https://doi.org/10.1121/1.401298.
Ohn, T.-L., Rutherford, M.A., Jing, Z., Jung, S., Duque-Afonso, C.J., Hoch, G., Picher, M.M., Scharinger, A., Strenzke, N., Moser, T., 2016. Hair cells use active zones with different voltage dependence of Ca^{2+} influx to decompose sounds into complementary neural codes. Proc. Natl. Acad. Sci. https://doi.org/10.1073/pnas.1605737113.
Paquette, S.T., Gilels, F., White, P.M., 2016. Noise exposure modulates cochlear inner hair cell ribbon volumes, correlating with changes in auditory measures in the FVB/nJ mouse. Sci. Rep. https://doi.org/10.1038/srep25056.
Peterson, A.J., Heil, P., 2018. A simple model of the inner-hair-cell ribbon synapse accounts for mammalian auditory-nerve-fiber spontaneous spike times. Hear. Res. https://doi.org/10.1016/j.heares.2017.09.005.
R Core Team, 2018. R: A Language and Environment for Statistical Computing.
Reijntjes, D.O.J., Lee, J.H., Park, S., Schubert, N.M.A., van Tuinen, M., Vijayakumar, S., Jones, T.A., Jones, S.M., Gratton, M.A., Xia, X.-M., Yamoah, E.N., Pyott, S.J., 2019. Sodium-activated potassium channels shape peripheral auditory function and activity of the primary auditory neurons in mice. Sci. Rep. 9, 2573. https://doi.org/10.1038/s41598-019-39119-z.
Reijntjes, D.O.J., Pyott, S.J., 2016. The afferent signaling complex: regulation of type I spiral ganglion neuron responses in the auditory periphery. Hear. Res. 336, 1–16. https://doi.org/10.1016/j.heares.2016.03.011.
Schindelin, J., Arganda-Carreras, I., Frise, E., Kaynig, V., Longair, M., Pietzsch, T., Preibisch, S., Rueden, C., Saalfeld, S., Schmid, B., Tinevez, J.Y., White, D.J., Hartenstein, V., Eliceiri, K., Tomancak, P., Cardona, A., 2012. Fiji: an open-source platform for biological-image analysis. Nat. Methods. https://doi.org/10.1038/nmeth.2019.
Schmiedt, R.A., 1989. Spontaneous rates, thresholds and tuning of auditory-nerve fibers in the gerbil: comparisons to cat data. Hear. Res. https://doi.org/10.1016/0378-5955(89)90115-9.
Sheng, M., Hoogenraad, C.C., 2007. The postsynaptic architecture of excitatory synapses: a more quantitative view. Annu. Rev. Biochem. https://doi.org/10.1146/annurev.biochem.76.060805.160029.
Taberner, A.M., Liberman, M.C., 2005. Response properties of single auditory nerve fibers in the mouse. J. Neurophysiol. https://doi.org/10.1152/jn.00574.2004.
Thévenaz, P., Unser, M., 2007. User-friendly semiautomated assembly of accurate image mosaics in microscopy. Microsc. Res. Tech. 70, 135–146.
Wickham, H., François, R., Henry, L., Müller, K., 2018. Dplyr: A Grammar of Data Manipulation.
Wickham, H., Henry, L., 2018. Tidyr: Easily Tidy Data with "Spread()" and "Gather()" Functions.
Winter, I.M., Robertson, D., Yates, G.K., 1990. Diversity of characteristic frequency rate-intensity functions in Guinea pig auditory nerve fibres. Hear. Res. https://doi.org/10.1016/0378-5955(90)90120-E.
Yin, Y., Liberman, L.D., Maison, S.F., Liberman, M.C., 2014. Olivocochlear innervation maintains the normal modiolar-pillar and habenular-cuticular gradients in cochlear synaptic morphology. JARO J. Assoc. Res. Otolaryngol. https://doi.org/10.1007/s10162-014-0462-z.
Zhang, L., Engler, S., Koepcke, L., Steenken, F., Köppl, C., 2018. Concurrent gradients of ribbon volume and AMPA-receptor patch volume in cochlear afferent synapses on gerbil inner hair cells. Hear. Res. https://doi.org/10.1016/j.heares.2018.03.028.